Journal of Applied Physics ARTICLE pubs.aip.org/aip/jap

Theory and computation of thermal-field emission from semiconductors

Cite as: J. Appl. Phys. **138**, 155705 (2025); doi: 10.1063/5.0284808
Submitted: 10 June 2025 · Accepted: 1 October 2025 ·
Published Online: 16 October 2025

View Online Export Citation CrossMark

Salvador Barranco Cárceles,[1,a)] Veronika Zadin,[2] Aquila Mavalankar,[3] Ian Underwood,[1] and Andreas Kyritsakis[2]

AFFILIATIONS

[1]School of Engineering, University of Edinburgh, Edinburgh, Scotland
[2]Institute of Technology, University of Tartu, Tartu, Estonia
[3]Adaptix Imaging Ltd., Oxford, England

[a)]**Author to whom correspondence should be addressed:** salvador.barranco-carceles@univ-lyon1.fr and s.barranco.carceles@gmail.com

ABSTRACT

Semiconducting field emitters present some interesting features (e.g., self-limited electron emission) for both scientific interest and industrial applications. The analysis of experimental results and device design has been restrained by the lack of accurate 3D models for the simulation of thermal-field emission from semiconductors. Here, we review and correct the equations of field emission from semiconductors and include them to expand GETELEC (General Tool for Electron Emission Calculations). Our method covers all electron emission regimes (field, thermal, and intermediate), aiming to maximize the calculation accuracy while minimizing the computational cost. GETELEC-2.0 is able to reproduce the characteristic non-linear I-V curves in Fowler–Nordheim coordinates obtained from semiconductors, giving insights about their nature, as well as providing an explanation to the lack of experimental observation of the field emitted valence band electrons from semiconductors.

I. INTRODUCTION

Semiconducting field emitters (s-FE) combine unique and appealing features such as self-limited emission[1] and superior photo-electron yield.[2] These make s-FE desirable for high specification technologies such as information displays,[3] ultrashort pulsed photon sources,[4] and portable 3D medical imaging devices.[5]

The widespread commercialization of field emission-based products remains elusive. This is due to the knowledge gap between field emission theory and experimental observations[6] and the resulting limited understanding about the emitter's surface dynamics, which makes the development of field emitter-based devices a challenging task. This gap is more acute for s-FE, given their higher complexity (presence of field penetration and surface states) when compared to metallic field emitters (m-FE).

Extensive work has been done to develop a model for field emission[7] and vacuum break down[8] in m-FE. Both models have provided a quantitative understanding of the behavior of metallic surfaces under high electrical fields (>5 V/nm). However, the fundamental study of field emission from semiconductors dates back to 1980.[9–12] Those studies are limited to 1D flat surfaces and do not consider the state-of-the-art field emission theory or the Nottingham and Joule heating effects on the emission. Therefore, data interpretation from recent semiconducting electron emitters (e.g., sharp emitters with tip radius <20 nm[13] or nanowires[14]) is expected to be inaccurate.

Accurate modeling and analysis tools will enable researchers to better understand the behavior of semiconducting emitters; thus, along with high-quality experimental data, bridging the knowledge gap between theory and experimental observations, and providing the basis for the effective design and realization of semiconducting field emission devices.

In this work, we develop a numerical model for the evaluation of the electron emission current density, Nottingham heating, and electron spectra from semiconducting emitters, based on Stratton's formulation[9,10,15] of the emission integrals from the conduction and valence bands. Our model is based on the existing computational software GETELEC-1.0,[7] which we expand here and update

into GETELEC-2.0 to include thermal-field emission from semiconductors, while maintaining the incorporation of emitter curvature effects.

GETELEC-2.0 allows the general and efficient calculation of the emission characteristics (current density, Nottingham heating, and electron spectra), which we then study for a wide range of emission parameters, contextualizing them to provide insights into the physics of semiconducting field emission devices.

The paper is organized as follows. In Sec. II, we give the theoretical framework of our model, deriving the mathematical expressions it uses (full derivation in the Appendix) and defining the relevant physical quantities and parameters. In Sec. III, we give a brief overview of the new numerical approach. In Sec. IV, we present the calculation results that provide insights about the emission physics from semiconductors and discuss the advantages and limits of our model. We finalize the paper by summarizing our findings and stating future research lines. (Note: the reader should be aware that the results shown here are qualitative since band bending has not been self-consistently calculated. However, the trends that the figures show are valid for *classical* semiconductors).

II. THEORY AND METHODS

A. General framework of the physics of field emission from semiconductors

Figure 1 shows the potential energy diagram of an n-type semiconductor under high electric fields. The bottom of the conduction band (E_C), the top of the valence band (E_V), the bandgap (E_g), the Fermi level (E_F), and the work function ($\phi = \chi + \zeta$) are given in eV. We set the vacuum energy (E_{vac}) at 0 eV, with negative energies going downward into the band. j_C and j_V are the emitted current density from the conduction and the valence band, respectively, in A/nm^2. The diagram also shows the potential barrier and its two components: the image potential (dotted curved line) and the potential due to the external electric field (solid straight line).

In metals, to a very good approximation and due to the large number of free charges, there is no potential drop in the emitter, i.e., the electric field does not penetrate the material. In semiconductors, in contrast, when a forward external field is applied (the emitter being the cathode), the field penetrates deep into the material bending the bands downward as the electrons accumulate on the surface of the material, as shown in Fig. 1. Therefore, the calculation of the electric field at the semiconductor surface requires a self-consistent solution of Poisson's equation (Fig. 2—blue loop) with the carrier concentration equations.

Upon the emission of a significant emission current density, the Fermi level also bends as the zero-current approximation becomes invalid.[11] To capture this change in E_F, another self-consistent loop (Fig. 2—green loop) to solve the continuity equation needs to be added to the calculation. Finally, as the emission grows exponentially, the emitter's temperature rises due to Joule and Nottingham effects, which results in the broadening of the Fermi–Dirac distribution. This effect modifies the number of charges available and the potential drop at the surface (see the above argument), and, thus, changing the energy distribution of the emitted electrons. The nature of the emission transits from field driven (cold) to temperature driven (hot) when the temperature

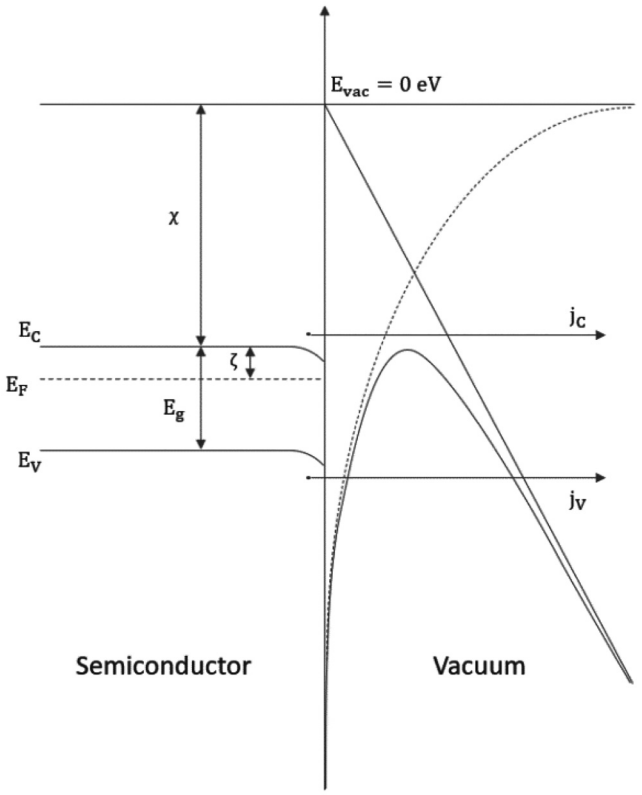

FIG. 1. Energy diagram of an n-type semiconductor under a high electric field for the zero current approximation (E_F constant for the semiconductor domain).

rises. Those effects require a third self-consistent loop (Fig. 2—red loop) that solves the head diffusion equation to accurately calculate the emission regime.

It is clear from the above analysis that field emission from semiconductors poses a highly coupled and non-linear problem that requires a holistic self-consistent solution for the entire emitter geometry to yield accurate solutions. This results in computationally heavy calculations due to the high dimensionality of the problem and the lack of analytical solutions. The first step to tackle this challenge is developing a numerical model that allows for the evaluation of the emitted current and Nottingham heating for any point in the parameter space. In this paper, we focus exactly on this first step. An analysis of the full self-consistent model of Fig. 2 will be given in a separate, forthcoming publication.

B. Equations of emission from semiconductors

Stratton[9] provided the first set of equations for electron emission from the conduction and valence bands. We start our analysis from Eq. (4) in Ref. 10, changing the nomenclature for clarity. Within the quasi-planar emitter approximation, we can treat the potential barrier as one-dimensional, thus ignoring the tangential dependence of the potential. Within this approximation, only the energy component normal to the emitting surface participates in

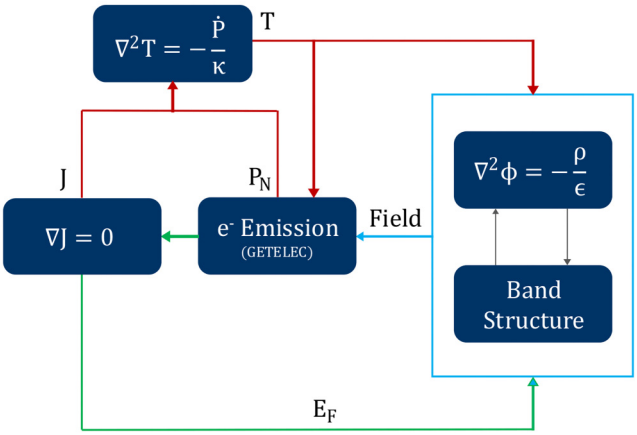

FIG. 2. Schematic of the effects involved in semiconductor field emitters and their dependencies.

tunneling. We define this energy component (normal components are denoted with the subscript "z" and tangential components with the subscript "r") as

$$E_z = E - E_r, \tag{1}$$

where E is the total energy of the electron and E_r is the tangential energy, with components E_x and E_y [see Appendix Eq. (A19)]. Now, we can calculate the emitted electron density from the conduction band by integrating over the momentum space in the band,

$$j_C = \frac{q}{4\pi^3\hbar^3}\int f_{FD}(E)D(E - E_r)f\frac{\partial E}{\partial p_z}d^3p, \tag{2}$$

where q is the electron charge, $\hbar$ is the reduced Plank constant, $f_{FD}(E)$ is the Fermi–Dirac distribution, and D(E) is the transmission coefficient given by the Kemble formula within the Jeffreys–Wentzel–Kramers–Brillouin (JWKB) approximation,[16]

$$D(E_z) = \frac{1}{1 + e^{G(E_z)}}, \tag{3}$$

with

$$G(E_z) = g\int_{z_1}^{z_2}\sqrt{U(z) - E_z}dz \tag{4}$$

and

$$U(z) = E_{vac} - qV(z) - \frac{Q}{z(1 + z/2R)} \tag{5}$$

as in Ref. 7 [see Eqs. (4)–(6)]. E and E_r correspond to

$$E = \frac{p^2}{2m^*}, \tag{6}$$

$$E_r = \frac{p_x^2 + p_y^2}{2m} = \frac{p_r^2}{2m}, \tag{7}$$

with m* as the effective and m as the free electron mass. Note that Eq. (7) originates from demanding the conservation of the transverse component of crystal momentum of the Bloch wave through the tunneling process. In our view, whether the crystal momentum p or the actual momentum $m\partial_p E$ should be conserved is an open question that goes beyond the scope of this paper. Here, we shall follow the standard approach in the literature for conserving p.

Conducting the transformations, Eq. (1) results in (see the Appendix for full development)

$$j_C = L\int_0 l_{FD}(E_z)(D(E_z) - \bar{\alpha}D(\bar{\alpha}E_z))dE_z, \tag{8}$$

where

$$L = \frac{qm}{2\pi^2\hbar^3}, \tag{9}$$

$$\bar{\alpha} = 1 - \frac{m^*}{m}, \tag{10}$$

$$l_{FD}(E_z) = -\ln\left(\frac{1}{1 + e^{\frac{E_z - E_F}{K_b T}}}\right). \tag{11}$$

Here, K_b is Boltzmann's constant (eV/K) and T is the temperature (K), with integration going from E_C to E_{vac}. Equation (8) is equivalent to Stratton's equation (7)[10] but with a slightly different notation.

From an intermediate step in the development of Eq. (8), we can extract the electron energy distribution of the emitted electrons as

$$J_C(E) = f_{FD}(E)\int_{\bar{\alpha}E}^{E} D(E_z)dE_z. \tag{12}$$

The conduction band component of the Nottingham heating can be calculated as

$$P_{N_C}(E) = \int_0 J_c(E)(E - E_R)dE, \tag{13}$$

where E_R is the energy of the replacement electrons.

Similarly, to the conduction band expression, we derive the current density for the valence band by performing integral manipulation in Eq. (14). It results in Eq. (15), which differs from Stratton's equation (A1).[15] This difference arises from a mathematical mistake in Stratton's derivation[10,15] (see the Appendix for details),

$$j_V = \frac{q}{4\pi^3\hbar^3}\int f_{FD}(\bar{E})D_V(\bar{E} + \bar{E}_r)\frac{\partial \bar{E}}{\partial p_z}d^3p, \tag{14}$$

$$j_V = L\int_{-\infty}^{E_V} l_{FD}(E_z)(D(E_z) - \bar{\alpha}D(\bar{\alpha}E_z - \alpha E_V))dE_z, \tag{15}$$

where

$$\alpha = \frac{m^*}{m}, \tag{16}$$

$$\bar{\alpha} = 1 + \frac{m^*}{m}. \tag{17}$$

Similar to what we did in Eq. (8), we can obtain the electron energy distribution for the valence band,

$$J_V(E) = f_{FD}(E) \int_{\bar{\alpha}E - \alpha E_V}^{E} D(E_z) dE_z, \tag{18}$$

from which we can develop the valence band emission contribution to the Nottingham heating,

$$P_{N_V}(E) = \int_0^E J_V(E)(E_R - E) dE. \tag{19}$$

III. CODE IMPLEMENTATION

The existing version of GETELEC-1.0 was based on using the appropriate formulas that can approximate both the values of the transmission coefficient D (E_z) and the integrals of the previous sections for various regimes. The tunneling barrier expression [Eq. (2.7) in Ref. 17] can be approximated by the following empirical formula:[7]

$$U(z) = F \frac{R(\gamma - 1)z + z^2}{\gamma z + R(\gamma - 1)}, \tag{20}$$

where F is the local electric field at the surface, R is the radii of the curvature (>10 nm since we do not take into account the quantum confinement effects), and γ is a parameter that corresponds to the ratio of the far field to the local one. In a recent work,[18] Kyritsakis showed that the barrier at any curved surface point can be approximated by an asymptotic expansion, with R being the radius of the *average* curvature at a given point. Equation (24) in Ref. 18 was specifically chosen to maintain this asymptotic behavior for $z \ll R$, but it also behaves well at large distances (the parabolic form would turn upward). The calculation of the transmission coefficient was done by the numerical integration of the JWKB formula based either on Eqs. (3) and (4), with the asymptotic formulas of Refs. 17 and 18 used when applicable for efficiency.

Then, the emission was based on the GTF model,[7,19] i.e., distinguishing various regimes based on the field and temperature, and applying appropriate approximations using a full numerical integration only when it is absolutely necessary. The issue is that a full numerical integration of both the JWKB integral and over energies is too computationally costly to be used in conjunction with large-scale models where the emission needs to be evaluated many times over many emission points. On the other hand, these integrals become far more complex for semiconductors and GTF-like approximations are not available.

To overcome this roadblock, in GETELEC-2.0, we follow a different computational approach. Within the new approach, the potential barrier is conceptually treated as independent of the emitter material. The shape of the barrier depends on three parameters: F, R, and γ. The Gamow function $G(E_z)$ also depends on these parameters. Our computational approach is to pre-calculate the function $G(E_z; F, R, \gamma)$ by numerically integrating Eq. (4) for various values of F, R, and γ and fit the $G(E_z)$ function to a fourth-order polynomial. Then, the coefficients of the polynomial along with the limits of validity of the polynomial approximation are tabulated and stored as an array. When a calculation is requested, the entire $D(E_z)$ function can be retried by interpolating the four polynomial coefficients, with its evaluation becoming very computationally efficient as it reduces to the evaluation of a fourth-order polynomial and an exponential. This new method allows the evaluation of any of the emission equations of the previous section at a very affordable computational cost, offering the generality and accuracy of the full numerical integration.

To validate the model, we calculate j and P_N by performing the full barrier calculation (GETELEC-1.0) and by the new computational approach (GETELEC-2.0). We calculated 8000 random combinations for F, R, T, ϕ, and γ over a broad range of values to ensure numerical accuracy and stability. Figure 3 shows the linear relation between the two methods for the range of current that is realistic to be measured on an experimental setup ($j > 10$ fA/nm^2).

Given the root-mean-square errors (RMSE) equal to 0.015 and 0.03 for the calculation of j and P_N, respectively, we are confident that our interpolation approach can be used as a general, accurate, and computationally efficient method to evaluate the emission characteristics, applicable to all regimes of thermal-field emission from parabolic bands. It can also be easily extendible to photo-emission and emission from materials with complex supply functions (e.g., semi-metals, molecules on surfaces, superconductors), given the appropriate equations.

IV. RESULTS

A. Electron energy distribution

GETELEC-2.0 has been used to simulate the field emission properties of intrinsic Germanium (i-Ge) with $E_C = -4.4$ eV, $E_F = -4.75$ eV (shown at 0 eV in the graphs), $E_g = 0.7$ eV, $m^*_e = 0.98$ m kg, and $m^*_h = 0.59$ m kg, where m is the free electron mass. F = 5 GV/m, R = 20 nm, and γ = 10. Three band positions have been simulated: (1) flatband as shown in Fig. 4 (left), (2) electron accumulation ($E_C = E_F$), and (3) semiconductor degeneracy ($E_C \ll E_F$), for a constant T = 300 K and for the zero-current approximation. For comparison, a metal point source has been also simulated (F = 5 GV/m, R = 20 nm, $\phi = -4.5$ eV, γ = 10, and T = 300 K).

The electron energy distribution of i-Ge (Fig. 4, right) shows the characteristic bandgap of the semiconductor, with the electrons from the conduction band in blue and from the valence band in orange. Both the conduction and valence distributions present a peak because of the combined effect of the density of states (DOS), tending to zero as it approaches E_C and E_V, and the Fermi–Dirac distribution (dotted black line in Fig. 4 left). The energy electron distribution of the metal emitter (blue) peaks around the Fermi

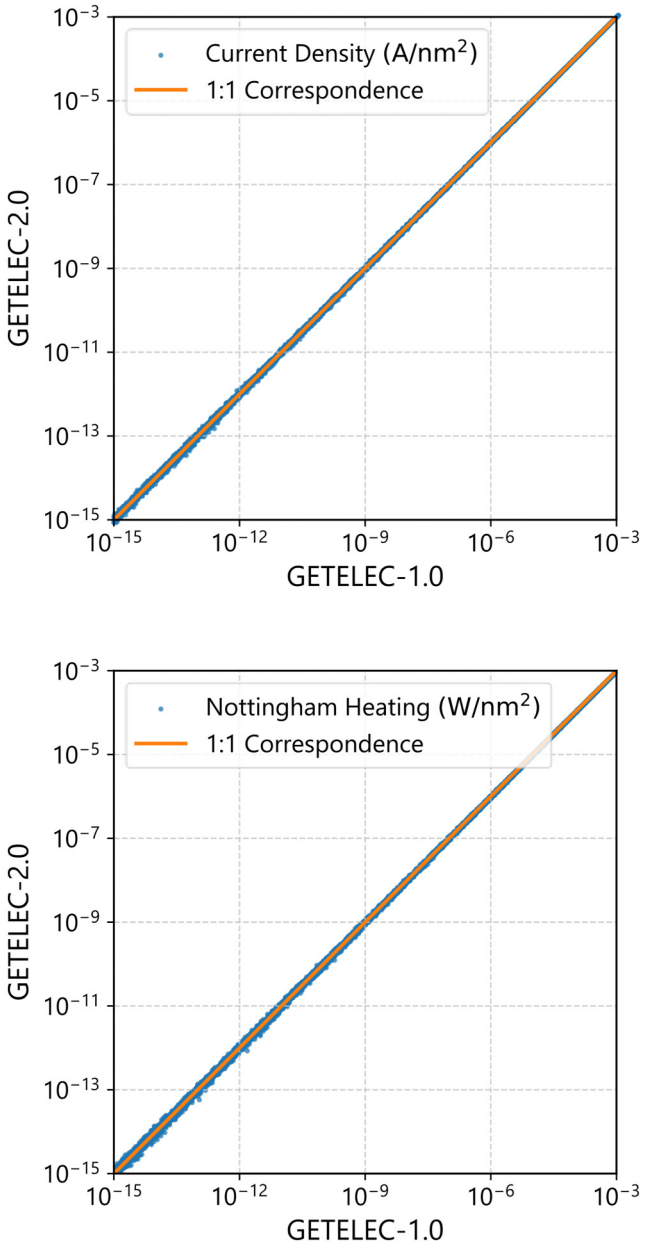

FIG. 3. Comparison of the current density (top) calculated by GETELEC-1.0 (full numerical calculation) and GETELEC-2.0 (interpolation method). The calculated Nottingham heating by both versions of GETELEC is also compared (bottom).

level, as a result of the combination of the Fermi–Dirac distribution and the transmission coefficient.

GETELEC-2.0 can be used to extract the potential barrier and the emitter surface temperature by fitting the right-hand side tail of $E_{V_{peak}}$ to the transmission coefficient D(E) and the left-hand side tail of $E_{C_{peak}}$ to the Fermi–Dirac distribution, respectively. The energy distribution between $E_{C_{peak}}$ and $E_{V_{peak}}$ yields information about the DoS, but such an analysis goes beyond the remit of this manuscript and will be addressed in the future.

However, obtaining high-quality data for analysis is not trivial, especially for semiconductors. In fact, to the knowledge of the authors, there are no reports for the experimental observation of either $E_{C_{peak}}$ and $E_{V_{peak}}$ or the semiconductor bandgap in field emission experiments. Our model suggests (Fig. 5) reasons for such a lack of experimental evidence, from which we can make suggestions for future experimental tests. We would like to notice that the bandgap and band peaks have been observed in photo-field emission experiments.[20]

At high electric fields, the electrons accumulate at the emitter surface degenerating the semiconductor; the point from which the emission from the semiconductor presents an energy distribution like that of a metal emitter [Fig. 5 blue line (metal) and orange line (degenerate semiconductor)]. This is consistent with the observation reported by Arthur on n-Ge.[21] However, it does not mean there is no emission from the valence band, but it has such a low magnitude in comparison with that of the emission from the conduction band that it is unlikely an electron energy analyzer has the high dynamic range required to measure both contributions.

As the field is reduced, less charge is accumulated at the surface relaxing the bands and transitioning from degeneracy to electron accumulation. From this point, the energy distribution is characteristic of that of a semiconductor with a sharp drop in the electron count (Fig. 5, green line) around the bandgap. The electron emission is still led by the conduction band, with emission from the valence band being three orders of magnitude lower. The valence band component is the leading emission term on the flat-band scenario. The dotted purple line (Fig. 5) shows the characteristic shape of valence distribution with sharp drop to the left where the bandgap is.

Figure 5 shows how the electron energy distribution goes from metal like, to conduction band led, to valence band led, as the field magnitude is reduced or the band bending is relaxed. The existence of a leading component makes the measurement of both peaks and bandgap of the electron energy distribution challenging because of the very wide dynamic range. Our model predicts a point at which the conduction and valence components have the same magnitude, which could be used to observe the bandgap in the emission characteristics. Such a point is discussed in Sec. IV B.

B. Emission characteristics and saturation

As explained in the previous section, at low electric fields, the bands can be considered as flat, and the valence component of the emission is dominant. With increasing fields, the valence component presents a slower growth compared to that of the conduction component. This slower growth is due to the fact that as the field increases and the potential barrier becomes thinner increasing the tunneling probability, the valence band is pushed down, removing electrons from high energy states, and thereby balancing both effects (Fig. 6, green line). On the other hand, as the conduction band is pushed down and approaches E_F, the number of electrons available for emission grows exponentially as per the Fermi–Dirac

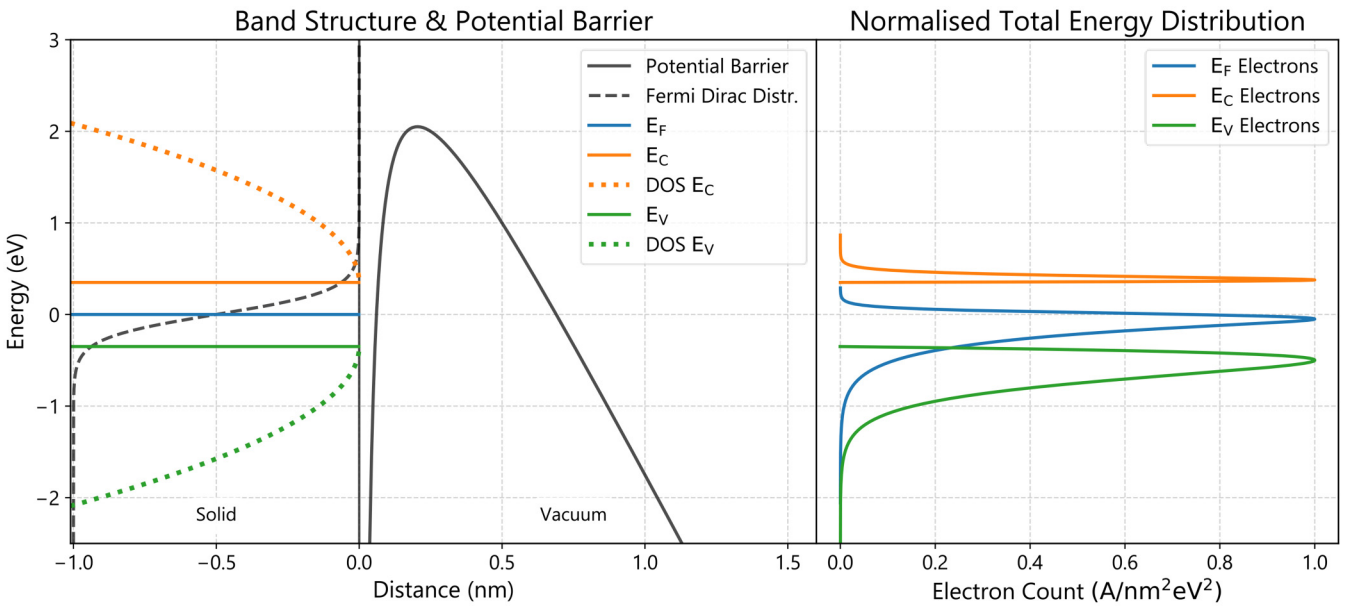

FIG. 4. Band structure and potential barrier (left, with $E_F = 0$ eV) and expected total energy distributions (TEDs) (right). In blue, the typical TED from a metal at T = 300 K with its peak slightly below E_F, Boltzmann tail above E_F, and Young tail below E_F. It can be seen that the Boltzmann tail is influenced by the Fermi–Dirac distribution (dotted black line) and the Young tail by the increasing width of the potential barrier (solid black line). For a semiconductor, two peaks are present: one from the conduction band (solid orange) and another from the valence band (solid green). The shape of these peaks is not only influenced by the Fermi–Dirac or the potential barrier, but also by the density of states (DOS). Thus, they show an abrupt fall near the bottom and top of the conduction and the valence bands, respectively.

distribution, and quickly takes over as the main contributor to the total emitted current (Fig. 6, orange and blue lines).

Such exponential growth continues until the emitter surface degenerates due to the accumulation of charges at the semiconductor's surface. At this point, the emission will predominantly come from around the Fermi level, like a metal (Fig. 5), and any further increase on the field results in voltage drop on the semiconductor with the bands being pushed down and, thus, emission saturation.

The slope of the valence band component (green) corresponds to the transmission coefficient, which remains monotonic over the range of simulated values. As the band is pushed down into deeper energy levels, the electron energy decreases, making G(E) to grow exponentially [see Eq. (3)]. Therefore, despite the fact that there are electrons available at the valence band, their associated tunneling probability quickly goes to zero and the emission component from the valence band vanishes. On the other hand, as the bands are pushed down, the conduction component of the emission (orange) grows. This represents the fact that more electrons become available for energies at which the tunneling probability is high. The slope of the conduction component is proportional to the Fermi–Dirac distribution, which remains static at the Fermi level. At the point where $E_C <\sim 2E_F$, the emission predominately comes from E_F and any further increase in the electric field will not yield more current. This saturation has been experimentally observed in p-type semiconductors.[1] Our model predicts that such saturation also occurs in n-type semiconductors, given that the emitter temperature remains constant, but no experimental evidence has been found yet.

The conduction component takes over the valence component at $E_C = E_F$, the point from which the emission exponentially grows until its saturation. Before that point, a threshold should be surpassed, until exponential growth is reached (Fig. 6). Such a behavior is analogous to that of a MOSFET.[22]

C. Heating effects

The Nottingham heating effect is defined as the net deposited/extracted energy due to the energy difference between the emitted and the replacing electrons. For metals with spherical isoenergetic Fermi surfaces, the average replacement electron energy is taken to be E_F, without any significant error.[2] For semiconductors, this is less clear since the replacement energy depends on the exact band structure and the doping level at a given position on the junction at the other side of the cathode.[23] For our model, we set the replacement energy to be at E_F, under the assumption that the quasi-Fermi level in the semiconductors is always defined to be close to the position of the vast majority of mobile electrons, which are the ones contributing to the current.

To show the dynamics of the Nottingham heating, we have plotted P_N for different band scenarios as we did for the electron energy (Fig. 7). At low fields, the emission is led by the valence band. Low energy electrons are emitted, to be replaced by high energy electrons, thus depositing energy that increases the emitter's temperature. As the field increases and the bands bend downward, the high energy electrons from the conduction band start tunneling

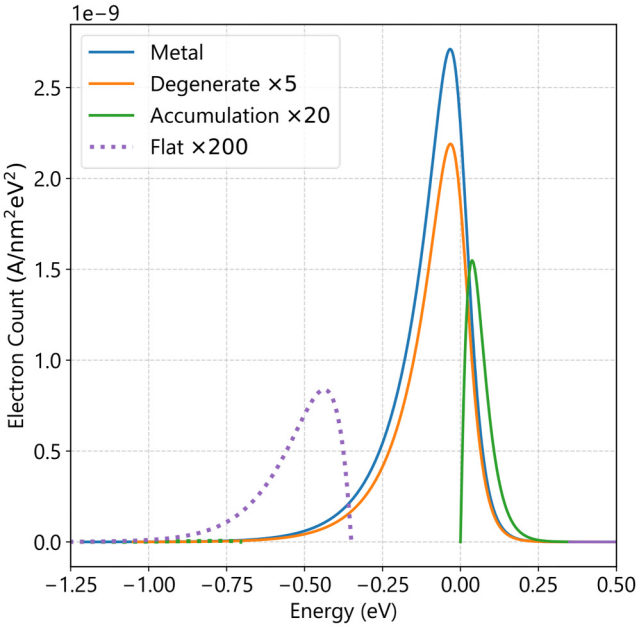

FIG. 5. Energy distribution of a metal emitter (blue), degenerate semiconductor (orange), electron accumulation (green), and flatband (purple) at T = 300 K (with $E_F = 0$ eV). The solid lines represent that the peak is from the conduction band and the dotted line from the valence band. Visualization proposes that the electron counts of the leading peaks have been multiplied by (×factor), and the ancillary peak (not shown) is at least three orders of magnitude smaller. It is evident that when the semiconductor degenerates, a metal-like peak is to be expected, but of lower magnitudes, as experimentally reported. The semiconducting character of the peaks appears in the low field regime.

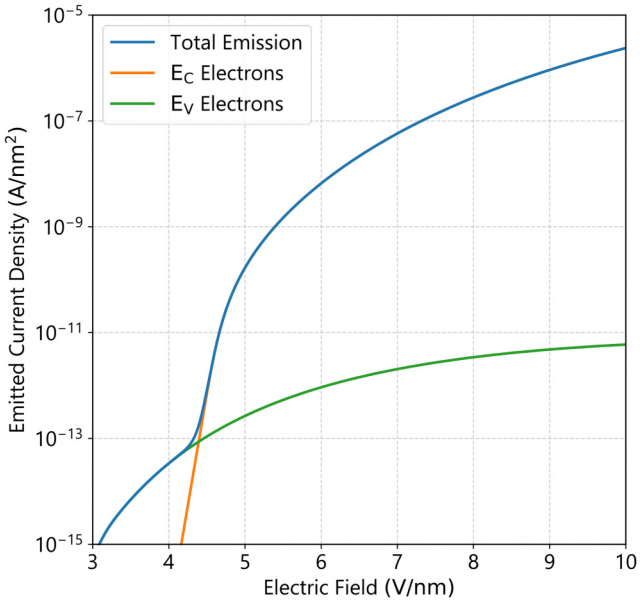

FIG. 6. Emitted current density (blue) as a function of the field, with the valence component (green) and the conduction band component (orange). The graph shows the saturation of both components in the high field regime and it indicates a point at which both valence and conduction components should have the same magnitude.

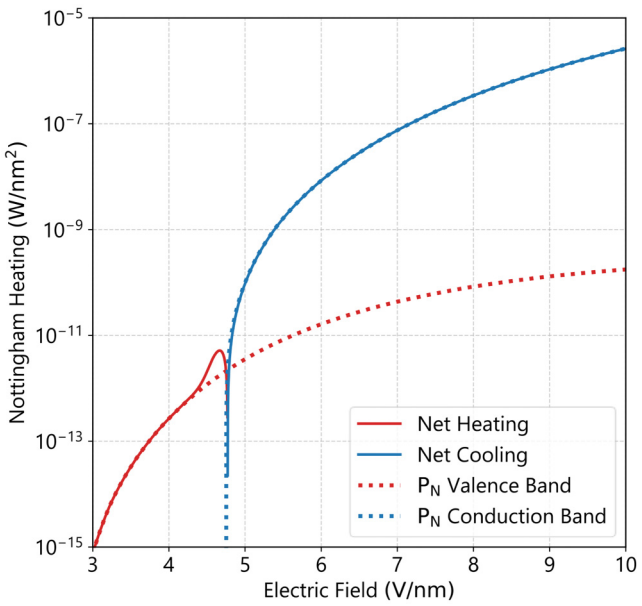

FIG. 7. Evolution of the Nottingham heating as a function of the electric field. The dotted lines represent the heating component from the valence band (red) and the conduction band (blue). The solid lines represent the net heating/cooling effect. The singularity ($F \approx 4.75$ V/nm) represents the transition from electron emission that heats up the emitter (most electrons from E_V) to emission that cools down the emitter (most electrons from E_C).

out of the semiconductor and, with them, extracting energy from the system, which results in a net cool down of the emitter's surface. This picture is consistent with that reported by Fursey in metal emitters, where the emitter surface is several degrees cooler than the emitter's core.[2]

D. Temperature dependence

Advances in field emission experimental setups have allowed to perform tests at cryogenic temperatures (<50 K).[24] While metals at those temperatures can behave like superconductors, semiconductors become insulators since no electrons have enough energy to populate the conduction band. Our model enables the study of field emission from cryogenic to high temperatures.

We have plotted (Fig. 8) the emitted current density for the flatband, accumulation, and degeneracy for temperatures ranging from 0 to 3000 K. We also show (Fig. 9) the corresponding electron energy distribution for the same band, same scenarios, and varying temperatures (0, 300, and 1000 K).

Figure 8 shows how the characteristic emitted current converges, regardless of the band structure, as the emitter temperature rises. This is due to the fact that at higher temperatures, more electrons become available at higher energies, and, thus,

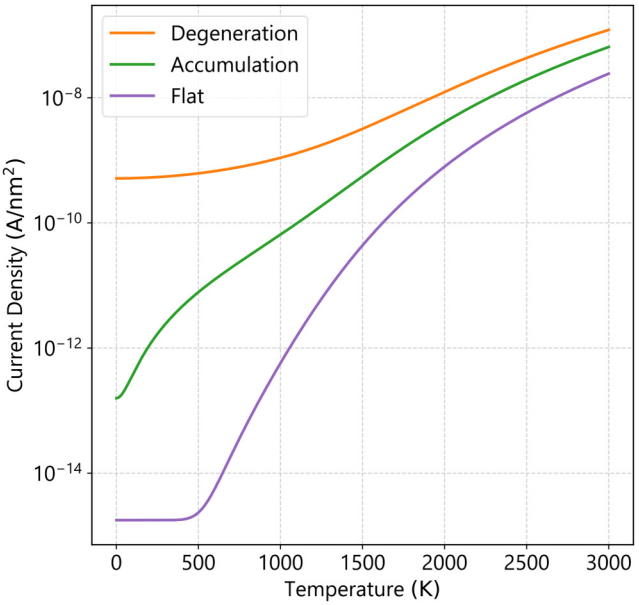

FIG. 8. Emitted current density as a function of temperature for a degenerated semiconductor (orange), for the accumulation regime (green), and for the flat-band scenario (purple). The sensitivity of electron emission from the semiconductor to temperature is apparent in the low temperature regime ($T < 1000$ K) with electron emission ranging over several orders of magnitude, with the exception of the degenerate line, which shows again its metal-like behavior. The emission lines converge at high temperatures as the emission becomes dominated by thermionic emission.

populating the states above E_C and broadening the Fermi–Dirac distribution. At that point, the electrons have enough energy to jump over the potential barrier, as expected in Schottky and thermionic emissions. This is clearly seen in Fig. 9, where the broadening of the E_C peak is observed at high temperatures (crosses vs triangles).

For the three band structures presented in Fig. 9, we see that the main component of the emitted electron is that from the conduction band (solid lines), with emission from the valence band (dotted lines) at least three orders of magnitude lower. For the flat (purple) and accumulation (green) cases, the left-hand side of the distribution tail quickly falls to zero as E_C is approached. While for the degeneracy case, we see a smooth tail which is proportional to the potential barrier, since E_C falls below E_F and the semiconductor degenerates (orange). The right-hand side of the peak is proportional to the Fermi–Dirac distribution at the calculated temperature. The differences in the full width half-maximum of the peaks represent the fact that at higher fields, the potential barrier gets thinner, which enables electrons to tunnel through, in addition to jumping over it. This picture is consistent with the previous findings in the literature.

At moderate temperatures (~300 K), we observe a similar electron distribution pattern than those at high temperatures. This is not the case at cryogenic temperatures (Fig. 9, circles), where there

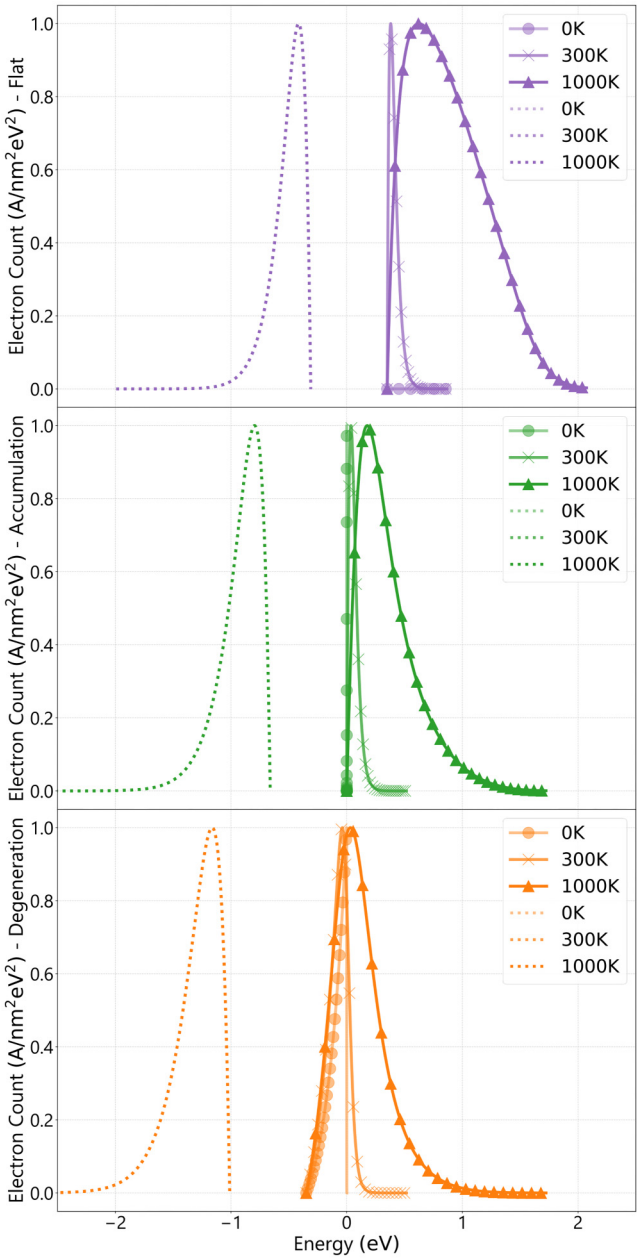

FIG. 9. Normalized electron total energy distribution from valence (dotted) and condition (solid) bands, for the flat (purple), accumulation (green), and degenerate (orange) regimes, as a function of temperature (clear circles for 0 K, translucid crosses for 300 K, and strong triangles for 1000 K, and $E_F = 0$ eV). The peaks shift with a growing field. The conduction peak is sensitive to temperature (broadening of the peak), while the valence peak remains temperature independent.

is a sharp drop in E_F, since there are no thermally excited electrons above it. In the low temperature regime, the emission predominantly comes from the valence band with holes drifting away from the surface and, thus, enabling conduction.

V. CONCLUSIONS

We have reviewed and corrected the mathematical expression for field emission from semiconductors. Our correction is for the electrons emitted from the valence band, which is of relevance at cryogenic temperatures.

GETELEC has been expanded to include the physics of field emission from semiconductors, both to calculate the emitted current density and Nottingham heating, given inputs such as the band structure, the electric field, and temperature of the emitter. The calculations of the Nottingham heating provide a qualitative picture since our code cannot calculate the energy distribution of the replacement electrons.

To improve the model's computational efficiency, we have implemented a novel approach to evaluate the potential energy barrier by polynomial fitting. This approach has increased the speed of our code by a factor of six, without sacrificing the numerical accuracy of the full JWKB method. We have also translated the code from Fortran to Python to make it more accessible and easier to use. A general tool for the calculation of field emission from semiconductors has been developed. The electron energy distribution of the emitted electrons can be calculated for a wide range of fields, temperatures, and band structures. Our model predicts the saturation of the emitted current density at high fields, regardless of the doping levels.

Despite its versatility and usefulness, the model has limitations: (1) The model is built treating the electrons as plane waves, which might not be an accurate approximation for small tip radii (R < electron wavelengths) and for non-parabolic band structures;[25] (2) In this work, our JWKB approximation of the 1D Schrödinger equation did not account for the transmission coefficient's dependence on transverse energy as reported in Ref. 26; (3) The model assumes a smooth emitter surface free of surface states, which might play an important role (e.g., negative electron affinity effects) in the electron emission from semiconductors as reported by Modinos;[12] (4) The energy of the replacement electrons to calculate the Nottingham heating is set to be the Fermi energy, since GETELEC cannot calculate it; for low field emission, these results have to be interpreted qualitatively; and (5) GETELEC provides the boundary condition for electron emission from semiconductors; to have a full picture of a semiconducting emitter, our model would have to be coupled with multi-physics packages to solve the continuity and heat equations. These limitations will be the focus of future research.

ACKNOWLEDGMENTS

S.B.C acknowledges support from the Royal Society of Edinburgh (Saltire Fellowship Grant No. 1956).

AUTHOR DECLARATIONS

Conflict of Interest

The authors have no conflicts to disclose.

Author Contributions

Salvador Barranco Cárceles: Conceptualization (lead); Formal analysis (supporting); Funding acquisition (lead); Investigation (equal); Software (equal); Writing – original draft (lead); Writing – review & editing (lead). **Veronika Zadin:** Writing – original draft (supporting). **Aquila Mavalankar:** Writing – original draft (supporting). **Ian Underwood:** Funding acquisition (supporting); Writing – original draft (supporting); Writing – review & editing (supporting). **Andreas Kyritsakis:** Conceptualization (supporting); Formal analysis (lead); Investigation (equal); Software (equal); Writing – original draft (supporting); Writing – review & editing (supporting).

DATA AVAILABILITY

The data that support the findings of this study are available from the corresponding author upon reasonable request. The code for the data presented in this study is openly available in Github at https://github.com/AndKyr/GETELEC, Ref. 27.

APPENDIX: MATHEMATICAL DEVELOPMENT OF FIELD EMISSION EQUATIONS

A. Emission equations for conduction band electrons

$$j_C = \frac{q}{4\pi^3\hbar^3}\int f_{FD}(E)D(E-E_r)\frac{\partial E}{\partial p_z}d^3p, \tag{A1}$$

where

$$E = \frac{p^2}{2m^*}, \tag{A2}$$

$$E_r = \frac{p_x^2+p_y^2}{2m} = \frac{p_r^2}{2m}, \tag{A3}$$

where m is the free electron mass of the electron and m* is the effective mass of the electron.

We first change to polar coordinates

$$p_r^2 = p_x^2 + p_y^2, \tag{A4}$$

$$\varphi = \tan^{-1}\frac{p_x}{p_y}, \tag{A5}$$

$$p_x = p_r\cos\varphi, \tag{A6}$$

$$p_y = p_r\sin\varphi, \tag{A7}$$

$$p_z = p_z, \tag{A8}$$

$$d^3p = p_r dp_r dp_z d\varphi. \tag{A9}$$

With all the above definitions,

$$j_C = \frac{q}{4\pi^3\hbar^3 m^*}\int_{-\infty}^{\infty}\int_0^{\infty}\int_0^{2\pi} f_{FD}(E)D(E-E_r)p_z p_r dp_r dp_z d\varphi. \tag{A10}$$

Since neither E nor E_r depends on the polar angle φ,

$$j_C = \frac{q}{2\pi^2\hbar^3 m^*}\int_{-\infty}^{\infty}\int_0^{\infty} f_{FD}(E)D(E-E_r)p_z p_r dp_r dp_z. \tag{A11}$$

Making a change of variables

$$\{p_z, p_r\} \rightarrow \{E, E_r\}, \tag{A12}$$

$$|\mathrm{Jac}| = \begin{vmatrix} \frac{\partial E}{\partial p_z} & \frac{\partial E}{\partial p_r} \\ \frac{\partial E_r}{\partial p_z} & \frac{\partial E_r}{\partial p_r} \end{vmatrix} = \begin{vmatrix} \frac{p_z}{m^*} & \frac{p_r}{m^*} \\ 0 & \frac{p_r}{m} \end{vmatrix} = \frac{p_z p_r}{m^* m}, \tag{A13}$$

$$p_z p_r dp_r dp_z = m^* m dE dE_r . \tag{A14}$$

Calculating the new integration limits

$$E = \frac{p_r^2 + p_z^2}{2m^*} = \frac{mE_r}{m^*} + \frac{p_z^2}{2m^*}. \tag{A15}$$

Since

$$\frac{p_z^2}{2m^*} \geq 0 \rightarrow E \geq \frac{m}{m^*} E_r \rightarrow E_r \leq \frac{m^*}{m} E = \alpha E, \tag{A16}$$

where

$$\alpha = \frac{m^*}{m}. \tag{A17}$$

So now, we have

$$j_C = \frac{mq}{2\pi^2 \hbar^3} \int_0^\infty \int_0^{\alpha E} f_{FD}(E) D(E - E_r) dE_r dE . \tag{A18}$$

Now, we define

$$E_z = E - E_r \rightarrow dE_z = -dE_r, \tag{A19}$$

$$\text{for } E_r = 0 \rightarrow E_z = E, \tag{A20}$$

$$\text{for } E_r = \alpha E \rightarrow E_z = \bar{\alpha} E, \tag{A21}$$

where

$$\bar{\alpha} = (1 - \alpha), \tag{A22}$$

$$L = \frac{mq}{2\pi^2 \hbar^3}. \tag{A23}$$

So,

$$\begin{aligned} j_C &= L \int_0^\infty f_{FD}(E) \int_E^{\bar{\alpha} E} -D(E_z) dE_z dE \\ &= L \int_0^\infty f_{FD}(E) \int_{\bar{\alpha} E}^E D(E_z) dE_z dE, \end{aligned} \tag{A24}$$

$$j_C = L \int_0^\infty -l'_{FD}(E) g(E) dE , \tag{A25}$$

where

$$g(E) = \int_{\bar{\alpha} E}^E D(E_z) dE_z . \tag{A26}$$

Solving by parts,

$$j_C = L \left[[l_{FD}(E) g(E)]_0^\infty + \left[\int_0 l_{FD}(E) g'(E) dE \right] \right], \tag{A27}$$

$$g'(E) = D(E) - \bar{\alpha} D(\bar{\alpha} E), \tag{A28}$$

and since

$$[l_{FD}(E) g(E)]_0^\infty = 0, \tag{A29}$$

we get

$$j_C = L \int_0 l_{FD}(E)(D(E) - \bar{\alpha} D(\bar{\alpha} E)) dE . \tag{A30}$$

From the later development, we can obtain the energy distribution of the electrons coming from the conduction band,

$$J_C = f_{FD}(E) \int_{\bar{\alpha} E}^E D(E_z) dE_z . \tag{A31}$$

B. Emission equations for valence band equations

$$j_V = \frac{q}{4\pi^3 \hbar^3} \int f_{FD}(\bar{E}) D_V(\bar{E} + \bar{E}_r) \frac{\partial \bar{E}}{\partial p_z} d^3 p , \tag{A32}$$

where

$$\bar{E} = E_v - \varepsilon , \tag{A33}$$

$$\varepsilon = E_V - E = E_V - \frac{p^2}{2m^*} = E_V - \frac{p_r^2 + p_z^2}{2m^*}, \tag{A34}$$

$$p_r^2 = p_x^2 + p_y^2 \#(A.35) , \tag{A35}$$

$$\bar{E}_r = \frac{p_r^2}{2m}, \tag{A36}$$

and with

$$D_V(E) = D(E_V - E), \tag{A37}$$

we get

$$\begin{aligned} D_V(\bar{E} + \bar{E}_r) &= D_V\left(E_V - E + \frac{p_r^2}{2m}\right) \\ &= D\left(E_V - E_V + E - \frac{p_r^2}{2m}\right) \\ &= D\left(E - \frac{p_r^2}{2m}\right). \end{aligned} \tag{A38}$$

Following the same reason for $f_{FD}(\bar{E})$, we get

$$f_{FD}(\bar{E}) = f_{FD}(E) , \tag{A39}$$

where m is the free electron mass of the electron and m* is the effective mass of the hole.

From all the above definitions, we obtain

$$j_V = \frac{q}{4\pi^3\hbar^3 m^*}\int f_{FD}(E)D\left(E - \frac{p_r^2}{2m}\right)p_z d^3p\,. \tag{A40}$$

Changing to polar coordinates, as done for j_c, we get

$$j_V = \frac{q}{2\pi^2\hbar^3 m^*}\int_{-\infty}^{\infty}\int_0^{\infty} f_{FD}(E)D\left(E - \frac{p_r^2}{2m}\right)p_z p_r dp_r dp_z\,. \tag{A41}$$

Making a change of variables,

$$\{p_z, p_r\} \rightarrow \{E, E_r\}\,, \tag{A42}$$

$$|\mathrm{Jac}| = \begin{vmatrix} \frac{\partial E}{\partial p_z} & \frac{\partial E}{\partial p_r} \\ \frac{\partial E_r}{\partial p_z} & \frac{\partial E_r}{\partial p_r} \end{vmatrix} = \begin{vmatrix} -\frac{p_z}{m^*} & -\frac{p_r}{m^*} \\ 0 & \frac{p_r}{m} \end{vmatrix} = -\frac{p_z p_r}{m^* m}, \tag{A43}$$

$$p_z p_r dp_r dp_z = -m^* m dE dE_r\,. \tag{A44}$$

Calculating the new integration limits

$$E = E_V - \frac{mE_r}{m^*} + \frac{p_z^2}{2m^*}. \tag{A45}$$

Since

$$E_r \geq 0 \rightarrow E \leq E_V - \frac{m}{m^*}E_r \rightarrow E_r \leq \frac{m^*}{m}(E_V - E) = \alpha(E_V - E), \tag{A46}$$

where

$$\alpha = \frac{m^*}{m}. \tag{A47}$$

So now, we have

$$j_V = \frac{mq}{2\pi^2\hbar^3}\int_{-\infty}^{E_V}\int_0^{\alpha(E_V - E)} f_{FD}(E)D(E - E_r)dE_r dE\,. \tag{A48}$$

Now, we define

$$E_z = E - E_r \rightarrow dE_z = -dE_r\,, \tag{A49}$$

$$\text{for} \quad E_r = 0 \quad \rightarrow E_z = E\,, \tag{A50}$$

$$\text{for} \quad E_r = \alpha(E_V - E) \quad \rightarrow E_z = \bar{\alpha}E - \alpha E_V, \tag{A51}$$

where

$$\bar{\alpha} = (1 + \alpha)\,, \tag{A52}$$

$$L = \frac{mq}{2\pi^2\hbar^3}. \tag{A53}$$

So,

$$j_V = L\int_{-\infty}^{E_V} f_{FD}(E)\int_{\bar{\alpha}E - \alpha E_V}^{E} D(E_z)dE_z dE\,, \tag{A54}$$

$$j_V = L\int_{-\infty}^{E_V} -l'_{FD}(E)g(E)dE\,, \tag{A55}$$

where

$$g(E) = \int_{\bar{\alpha}E - \alpha E_V}^{E} D(E_z)dE_z\,. \tag{A56}$$

Solving by parts,

$$j_V = L\left[\left[-l_{FD}(E)g(E)\right]_{-\infty}^{E_V} + \left[\int_{-\infty}^{E_V} l_{FD}(E)g'(E)dE\right]\right], \tag{A57}$$

$$g'(E) = D(E) - \bar{\alpha}D(\bar{\alpha}E - \alpha E_V)\,, \tag{A58}$$

and since

$$[-l_{FD}(E)g(E)]_{-\infty}^{E_V} = 0, \tag{A59}$$

we get (with E_V as the upper limit)

$$j_V = L\int_{-\infty}^{E_V} l_{FD}(E)(D(E) - \bar{\alpha}D(\bar{\alpha}E - \alpha E_V))dE\,, \tag{A60}$$

which contrasts with Stratton's

$$j_V = L\int_{-\infty}^{E_V} l_{FD}(E)(D(E) - \bar{\alpha}D(\bar{\alpha}E - \alpha E_V))dE + \ln\left\{1 + e^{\frac{E_V}{kT}}\right\}\int_{E_V}^{\bar{\alpha}} D(E)dE\,. \tag{A61}$$

From the later development, we can obtain the energy distribution of the electrons coming from the conduction band

$$J_V = f_{FD}(E)\int_{\bar{\alpha}E - \alpha E_V}^{E} D(E_z)dE_z\,. \tag{A62}$$

REFERENCES

[1] M. Choueib, R. Martel, C. S. Cojocaru, A. Ayari, P. Vincent, and S. T. Purcell, "Current saturation in field emission from H-passivated Si nanowires," ACS Nano **6**(8), 7463–7471 (2012).

[2] G. Fursey, *Field Emission in Vacuum Microelectronics* (Kluwer Academic, 2003).

[3] S. B. Cárceles, A. Kyritsakis, V. Zadin, A. Mavalankar, and I. Underwood, "27-2: field emission beyond information displays," in *Digest of Technical Papers—SID International Symposium* (John Wiley & Sons Inc., 2023), pp. 366–369.

[4] M. E. Swanwick, P. D. Keathley, F. X. Kartner, and L. F. Velasquez-Garcia, "Ultrafast photo-triggered field emission cathodes using massive, uniform arrays of nano-sharp high-aspect-ratio silicon structures," in *2013 Transducers and Eurosensors XXVII: The 17th International Conference on Solid-State Sensors, Actuators and Microsystems, TRANSDUCERS and EUROSENSORS 2013* (IEEE, 2013), pp. 2680–2683.

[5] G. Travish, F. J. Rangel, M. A. Evans, K. Schmiedehausen, and B. Hollister, "Addressable flat-panel x-ray sources for medical, security, and industrial applications," Proc. SPIE **8502**, 85020L (2012).

[6]A. Ayari *et al.*, "All field emission experiments are noisy, … are any meaningful ?," J. Vac. Sci. Technol. B **41**, 024001 (2023).
[7]A. Kyritsakis and F. Djurabekova, "A general computational method for electron emission and thermal effects in field emitting nanotips," Comput. Mater. Sci. **128**(4), 15–21 (2017).
[8]X. Gao *et al.*, "Molecular dynamics simulations of thermal evaporation and critical electric field of copper nanotips," J. Phys. D: Appl. Phys. **53**, 365202 (2020).
[9]R. Stratton, "Field emission from semiconductors," Proc. Phys. Soc. B **68**(10), 746–757 (1955).
[10]R. Stratton, "Theory of field emission from semiconductors," Phys. Rev. **125**(1), 67–82 (1962).
[11]L. M. Baskin, O. I. Lvov, and G. N. Fursey, "General features of field emission from semiconductors," Phys. Status Solidi B **47**(1), 49–62 (1971).
[12]A. Modinos, *Field, Thermionic, and Secondary Electron Emission Spectroscopy* (Springer US, Boston, MA, 1984), Vol. 102.
[13]A. Kyritsakis and J. P. Xanthakis, "Extension of the general thermal field equation for nanosized emitters," J. Appl. Phys. **119**(4), 045303 (2016).
[14]M. Choueib, A. Ayari, P. Vincent, M. Bechelany, D. Cornu, and S. T. Purcell, "Strong deviations from Fowler–Nordheim behavior for field emission from individual SiC nanowires due to restricted bulk carrier generation," Phys. Rev. B **79**(7), 075421 (2009).
[15]R. Stratton, "Energy distributions of field emitted electrons," Phys. Rev. **135**(3A), A794–A805 (1964).
[16]E. C. Kemble, "A contribution to the theory of the B. W. K. method," Phys. Rev. **48**, 549–561 (1935).
[17]A. Kyritsakis and J. P. Xanthakis, "Derivation of a generalized Fowler–Nordheim equation for nanoscopic field-emitters," Proc. R. Soc. A **471**(2174), 20140811 (2015).
[18]A. Kyritsakis, "General form of the tunneling barrier for nanometrically sharp electron emitters," J. Appl. Phys. **133**(11), 113302 (2023).
[19]K. L. Jensen, "General formulation of thermal, field, and photoinduced electron emission," J. Appl. Phys. **102**(2), 024911 (2007).
[20]C. Bandis and B. B. Pate, "Simultaneous field emission and photoemission from diamond," Appl. Phys. Lett. **69**(3), 366–368 (1996).
[21]J. R. Arthur, *Energy Distribution of Field Emission From Germanium* (North-Holland Publishing Co, 1964).
[22]S. M. Sze and K. K. Ng, *Physics of Semiconductor Devices* (Wiley-Interscience, 2007).
[23]M. S. Chung, Y. J. Jang, A. Mayer, P. H. Cutler, N. M. Miskovsky, and B. L. Weis, "Energy exchange in field emission from semiconductors," J. Vac. Sci. Technol. B **26**(2), 800–805 (2008).
[24]M. Jacewicz, J. Eriksson, R. Ruber, S. Calatroni, I. Profatilova, and W. Wuensch, "Temperature-dependent field emission and breakdown measurements using a pulsed high-voltage cryosystem," Phys. Rev. Appl. **14**(6), 061002 (2020).
[25]V. V, K. V, and S. M. A. Mitin, *Quantum Heterostructures: Microelectronics and Optoelectronics* (Cambridge University Press, 1999).
[26]N. Hernandez *et al.*, "A scattering matrix approach to the effective mass dependence of tunneling current through heterojunctions," J. Appl. Phys. **136**(15), 155704 (2024).
[27]"GETELEC: General tool for electron emission calculations," Github, https://github.com/AndKyr/GETELEC (2025).